

## Forecasting severe convective storms with WRF-based RTFDDA radar data assimilation in Guangdong, China



Yongjie Huang<sup>a</sup>, Yubao Liu<sup>a,c,\*</sup>, Mei Xu<sup>a</sup>, Yuwei Liu<sup>a</sup>, Linlin Pan<sup>a</sup>, Haoliang Wang<sup>a</sup>, Will Y.Y. Cheng<sup>a</sup>, Ying Jiang<sup>b</sup>, Hongping Lan<sup>b</sup>, Honglong Yang<sup>b</sup>, Xiaolin Wei<sup>b</sup>, Rong Zong<sup>b</sup>, Chunyan Cao<sup>b</sup>

<sup>a</sup> National Center for Atmospheric Research (NCAR), Boulder, CO, USA

<sup>b</sup> Meteorological Bureau of Shenzhen Municipality, Shenzhen 518040, China

<sup>c</sup> Chinese Electric Power Research Institute, Beijing, China

### ARTICLE INFO

#### Keywords:

Severe convective storms  
RTFDDA  
Radar data assimilation  
Latent heating  
Nowcasting

### ABSTRACT

Radar data assimilation is an important method for short-term convection forecasting or nowcasting. To improve the short-term (mainly 0–3 h) precipitation forecasts for severe convective storms, an analysis nudging (Newtonian relaxation) based hydrometeor and latent heat nudging (HLHN) technique was developed to effectively assimilate radar reflectivity data in a Weather Research and Forecasting (WRF)-based real time four-dimensional data assimilation and short-term forecasting system (RTFDDA). The purpose of this study is to investigate the performance of the RTFDDA system with radar data assimilation (RTFDDA-RDA) with rapid-cycling forecasting applications for Shenzhen, a subtropical coastal metropolis in southern China. The RTFDDA-RDA system was run to produce hindcasts for ten severe convective storm events occurred in Guangdong region during the 2017 rainy season. Results show that, through nudging cloud hydrometeors retrieved from radar reflectivity and the associated latent heat release, RTFDDA-RDA is able to produce the meso- and convective-scale features of the convective storms in a good accuracy and improve the short-term precipitation forecasting of the convective storms. Subjective and statistical evaluation results demonstrate that RTFDDA-RDA presents a reasonable capability for forecasting convective systems with improving the initial conditions and resulting in significant improvements of precipitation forecasting skills, especially for the 0–3-h nowcasting range. The sensitivity experiments on different latent heating schemes show that, the convective-stratiform separated heating scheme has the best performance of forecasts. Finally, intercomparison of different radar data assimilation approaches will be conducted in future.

### 1. Introduction

Weather radar measures the wind fields and microphysical properties of convective storms with high spatiotemporal resolution, which is very useful for forecasting of severe convective weather. As lots of previous studies show, numerical weather prediction (NWP) models always fail to replicate radar observations to high precision (Min et al., 2015; Lompar et al., 2017, 2018). Radar data assimilation (RDA) has been an important approach for improving NWP models' skills in short-term convection forecasting or nowcasting. Currently, there are several methods to assimilate radar data (reflectivity or radial wind) into numerical models, such as three-dimensional variational data assimilation (3DVAR, Xiao et al., 2005; Sugimoto et al., 2009; Gao and Stensrud, 2012; Wang et al., 2013a; Vendrasco et al., 2016), four-dimensional

variational data assimilation (4DVAR, Sun and Crook, 1997; Sun, 2005; Sun and Wang, 2013; Wang et al., 2013b), ensemble Kalman filter (EnKF, Snyder and Zhang, 2003; Tong and Xue, 2005; Zhang et al., 2009; Dowell et al., 2011), and Newtonian relaxation-based nudging method (Haase et al., 2000; Stephan et al., 2008; Xu et al., 2013).

The nudging method makes gradual, incremental adjustments to the model state variables based on the departure of the model state from observations. There are several algorithms to nudge radar data into convective-scale NWP models. For example, Stephan et al. (2008) derived surface precipitation rates from radar reflectivity data and applied latent heat nudging based on the surface precipitation rate to improve very short-range convective-scale forecasts. Korsholm et al. (2015) proposed a new approach to assimilate two-dimensional radar-derived precipitation into a high-resolution NWP model, in which a nudging

\* Corresponding author at: National Center for Atmospheric Research (NCAR), Boulder 80301, CO, USA.  
E-mail address: [yliu@ucar.edu](mailto:yliu@ucar.edu) (Y. Liu).

term is added to the horizontal velocity divergence tendency equation based on the offset between radar-derived precipitation and model precipitation.

Developed at NCAR/RAL, RTFDDA is a WRF-based real-time four-dimensional data assimilation and short-term forecasting system that effectively assimilates diverse observations for real-time NWP (Liu et al., 2008a, 2008b). To improve the short-term precipitation forecasts for severe convective storms, an analysis nudging (Newtonian relaxation)-based hydrometeor and latent heat nudging (HLHN) technique was developed to assimilate radar reflectivity data in RTFDDA (Xu et al., 2013). The RTFDDA system with radar data assimilation (RTFDDA-RDA) has been running operationally at the U.S. Army test ranges. The forecast experiments show that the hourly accumulated precipitation forecast skill from the experiment with RTFDDA-RDA is significantly higher than that without radar reflectivity assimilation, especially in the first 5 h (Xu et al., 2013; Sun et al., 2014). A RTFDDA-RDA system was deployed and running operationally in Meteorological Bureau of Shenzhen Municipality, China. The system assimilates three-dimensional mosaic radar reflectivity and provides operational hourly-cycled analysis and short-term (mainly 0–3 h) forecasting of convection.

The RTFDDA-RDA has been continuously adjusted and improved in the last a few years. The nudging-based radar data assimilation method has several advantages, including its ability to adjust the model convection according to the full-physics model dynamical and physical equations for dynamical and physical consistency, and high computation efficiency. The limitations of the approach include its dependency on empirical relationships between the hydrometeor variables and observed radar reflectivity, and empirical determination of nudging parameters. A crucial aspect of the latent heat nudging is the prescription of the heating or cooling rates based on the radar reflectivity. Given the mismatch of the observed and model-simulated storm locations and the complexity of the microphysical and dynamical processes, it remains obscure where in space and time and how much heating/cooling should be applied in order to best correct the model errors. Several assumptions are adopted by operational centers. For example, the High-Resolution Rapid Refresh (HRRR) model, an operational rapid update model of the National Weather Service since 2014, assimilates radar reflectivity and reflectivity derived from lightning data via a radar-DFI-latent-heating technique, and it adds latent heating estimated from observed reflectivity only in the regions where the observed reflectivity is greater than a threshold (Benjamin et al., 2016). The reflectivity threshold is uncertain and sensitive, and varies in different versions of HRRR (Bytheway et al., 2017). A different latent heat nudging approach is developed in the COSMO-DE model (Stephan et al., 2008), where the nudging latent heat tendency is determined from the model latent heat tendency and the ratio of radar-estimated surface precipitation rate to model surface precipitation rate.

This paper intends to explore the forecast sensitivities with respect to the heating and cooling schemes of the RTFDDA-RDA system deployed at Shenzhen, a sub-tropical coastal metropolis in southern China. The impact of latent heat nudging schemes with both heating and cooling and only heating respectively is examined through careful analyses of a case study of coastal rainbands. A new latent heating scheme, with differential heating rates for the convective and stratiform regions, is developed. In addition to the case study, the RTFDDA-RDA system was run to produce hindcasts for ten severe convective storms that occurred in Guangdong region during the rainy season in 2017. The next section describes the RTFDDA-RDA methodology and model experiment design. Results and verification of a case study with a single forecast cycle are presented in Section 3. Statistical evaluation of the RTFDDA-RDA forecast skills for the ten convection weather events with hourly forecast cycles is presented in Section 4. Discussions and conclusions are given in Sections 5 and 6, respectively.

## 2. Methodology and model setups

### 2.1. Data assimilation scheme

The radar data assimilation scheme used in this study is grid-nudging based, where hydrometeor and latent heat nudging (HLHN) is performed on each grid point of the model (Xu et al., 2013). The radar data here are the three-dimensional gridded mosaic dataset for the southern China region, merged from several individual radars. The data mapping is provided by Meteorological Bureau of Shenzhen Municipality, China. The mosaic radar datasets are updated every 12 min. The mosaic reflectivity is firstly interpolated to the model grids in the 9- and 3-km fine mesh domains. Then empirical relationships between radar reflectivity  $Z$  and rain water/snow mixing ratio  $Q_r/Q_s$  (i.e.  $Z - Q_r$  ( $Z - Q_s$ ) relationships) are used to estimate  $Q_r$  ( $Q_s$ ) from the reflectivity on the model grids. They are  $Z_r = 95.6 + 17.5\log_{10}(\rho Q_r)$  when the temperature is warmer than 0 °C and  $Z_s = 83.6 + 17.5\log_{10}(\rho Q_s)$  when the temperature is cooler than 0 °C, respectively (Stoelinga, 2005). Here  $\rho$  is air density (units of  $\text{kg m}^{-3}$ ). The reflectivity ( $Z_r/Z_s$ ) is in units of dBZ, and rain water/snow mixing ratio ( $Q_r/Q_s$ ) is in units of  $\text{kg kg}^{-1}$ .

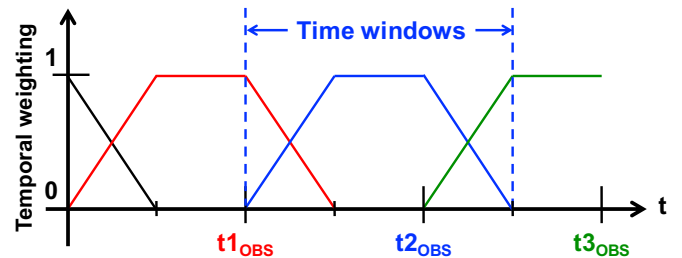
In HLHN, the model mixing ratios of rain water and snow are nudged toward the radar-retrieved three-dimensional  $Q_r$  and  $Q_s$  during the integration of the rain water and snow prognostic equations. Meanwhile, the corresponding latent heating or cooling is also added to the WRF thermodynamic (temperature) equation. The simplified equations in the nudging scheme are as follows,

$$\frac{\partial Q_x}{\partial t} = -\vec{V} \cdot \nabla Q_x + S_{Q_x} + w_1(Q_x^{obs} - Q_x^{mod}) \quad (1)$$

$$\frac{\partial T}{\partial t} = -\vec{V} \cdot \nabla T + S_T + w_2 \frac{\sum L_x \Delta Q_x}{C_p} \quad (2)$$

$$\Delta Q_x = w_1(Q_x^{obs} - Q_x^{mod}), x \in (r, s) \quad (3)$$

where  $Q_x$  ( $Q_x^{obs}$  and  $Q_x^{mod}$ ) represent the observation and model variables, respectively) is the mixing ratio of rain water or snow,  $S_{Q_x}$  is the source of mixing ratio from physical processes (microphysical conversion processes, land surface moisture flux, mixing, diffusion, etc.),  $S_T$  is the source of air temperature from physical processes (latent heating, sensible heating, etc.),  $L_x$  is specific latent heat, and  $C_p$  is the specific heat of air at constant pressure. The third terms of the right-hand side in the Eqs. (1) and (2) are the nudging terms of hydrometeor mixing ratio and latent heat, respectively. And  $w_1$  and  $w_2$  are nudging weighting coefficients of hydrometeor mixing ratio and latent heat, respectively. The weighting coefficient  $w_1$  is a product of nudging coefficient (inverse of nudging time scale), temporal weighting and spatial weighting. The temporal weighting function depicting the assimilation time window affected by any given radar observation is shown in Fig. 1. When a radar echo is observed, cloud development and latent heat release have already occurred. Therefore, maximum temporal weights are applied at

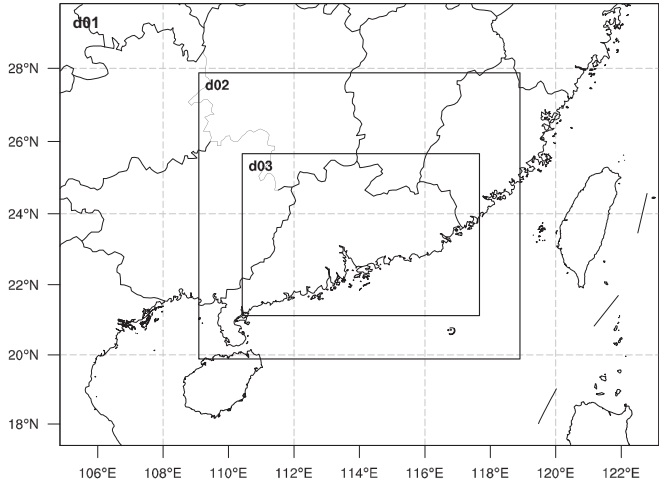
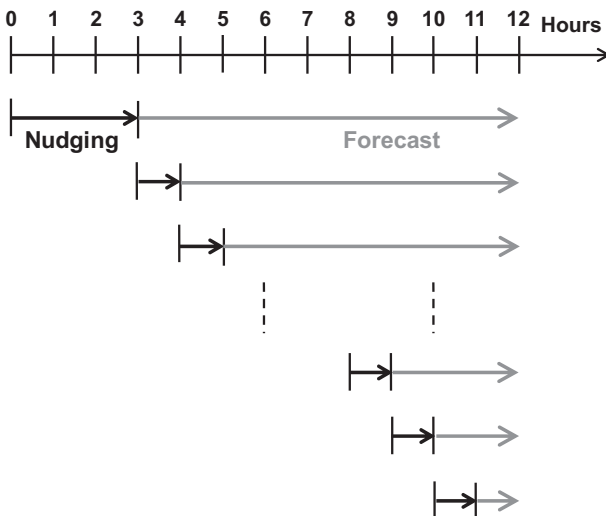


**Fig. 1.** Temporal weighting function for assimilation of radar observations.  $t1_{OBS}$ ,  $t2_{OBS}$ , and  $t3_{OBS}$  mark the observations time and the color shades are temporal weights corresponding to the observation in the same color. In this study, the intervals between two successive radar observations are 12 min. The time window for each radar observation is 18 min.

**Table 1**

Severe convective storms and their time periods selected in this study.

Events	Event period (UTC, 12 h)	Convection types
CASE01	2017-04-21_00:00–04-21_12:00	Squall lines
CASE02	2017-05-03_18:00–05-04_06:00	Squall lines
CASE03	2017-05-15_09:00–05-15_21:00	Multi-cell cluster storms
CASE04	2017-06-15_12:00–06-16_00:00	Multi-cell cluster storms
CASE05	2017-06-16_03:00–06-16_15:00	Multi-cell cluster storms
CASE06	2017-06-18_21:00–06-19_09:00	Multi-cell cluster storms
CASE07	2017-07-17_06:00–07-17_18:00	Multi-cell cluster storms
CASE08	2017-08-03_18:00–08-04_06:00	Multi-cell cluster storms
CASE09	2017-08-22_06:00–08-22_18:00	Multi-cell cluster storms affected by Typhoon HATO (1713)
CASE10	2017-08-26_18:00–08-27_06:00	Mesoscale spiral bands of Typhoon PAKHAR (1714)

**Fig. 2.** Model domain configuration. The horizontal grid sizes of d01, d02 and d03 are 27, 9 and 3 km, respectively.**Fig. 3.** Schematics of radar data assimilation and forecast experiment schedule. The black thick solid arrows represent the nudging periods, and the gray thick solid arrows represent forecast periods.

the simulation time before the actual observation time. In the RTFDDA-RDA system, the weighting coefficient of latent heat nudging,  $w_2$ , is tunable. Its functional forms with respect to regions of latent heating or cooling, convective or stratiform precipitations, are subjects of the sensitivity experiments in this study. The details of the sensitivity experiments design are described in the next section.

**Table 2**

Sensitivity experiments on the latent heating scheme.

Experiments	Description
NO_RDA	Model forecast without radar data assimilation
RDA_HC	Equivalent heating and cooling weighting, namely $w_2 = 1$
RDA_H	Just heating and neglect cooling, namely $w_2 = 1$ only when $\Delta Q_x > 0$ in the Eq. (2), else $w_2 = 0$
RDA_CS	Use convective-stratiform separated heating scheme, detail in Section 2.2

## 2.2. Model configuration and case description

Ten severe convective storms occurred in Guangdong Province, China, during the 2017 flood season are selected in this study. The RTFDDA-RDA version used here is based on the Weather Research and Forecasting model (WRF), version 3.8.1. For each storm event, a 12-h period, which roughly covers the lifecycles of the major convection storms in the study domain, is selected for the modeling study. The periods and descriptions for all the ten events are given in Table 1. The model is configured with three nested-grid domains at 27-, 9-, and 3-km horizontal grid spacings, respectively (Fig. 2). The Thompson microphysical parameterization scheme (Thompson et al., 2008) is used in all domains, and Grell-Freitas cumulus parameterization scheme (Grell and Freitas, 2014) is used in the 27- and 9-km grid domains. No cumulus scheme is activated in the 3-km grid domain. The other physical parameterization schemes are the same in the three domains, including Yonsei University PBL physics scheme (Hong et al., 2006), RRTMG longwave and shortwave radiation scheme (Iacono et al., 2008), and Unified Noah land surface scheme (Tewari et al., 2004). The model initial and boundary conditions are driven from the NCEP-GFS data (0.5-degree resolution, <https://nomads.ncdc.noaa.gov/data/gfs4>). Radar data are assimilated in the 9- and 3-km domains. The data assimilation and forecast timelines are schematically shown in Fig. 3. The model firstly assimilated the radar data at 12-min intervals for 3 h, and then was integrated to generate 9 h forecasts. Henceforth, the hourly assimilation and forecast cycles started from the third hour, and the last cycle run assimilated radar data for 11 h and generated 1 h forecast (Fig. 3).

For each severe storm event, a RTFDDA run without radar data assimilation, NO\_RDA, is first conducted as the control experiment, which is used as a baseline for evaluating the impact of radar data assimilation. Then three RTFDDA-RDA sensitivity experiments are conducted using different settings of the weighting coefficient of latent heat nudging ( $w_2$ ) (Table 2). The setups of the three RDA sensitivity experiments are as follows: the first experiment, RDA\_HC, uses equivalent weights for heating and cooling (i.e.,  $w_2 = 1$  in both regions of  $\Delta Q_x > 0$  and  $\Delta Q_x < 0$ ); the second experiment, RDA\_H, includes only latent heating but not cooling (i.e.,  $w_2 = 1$  for  $\Delta Q_x > 0$ , and  $w_2 = 0$  for  $\Delta Q_x < 0$ ) considering cooling will disturb the dynamic fields of convective system when the storm locations are different between observation and model forecast; and in the third experiment, RDA\_CS,

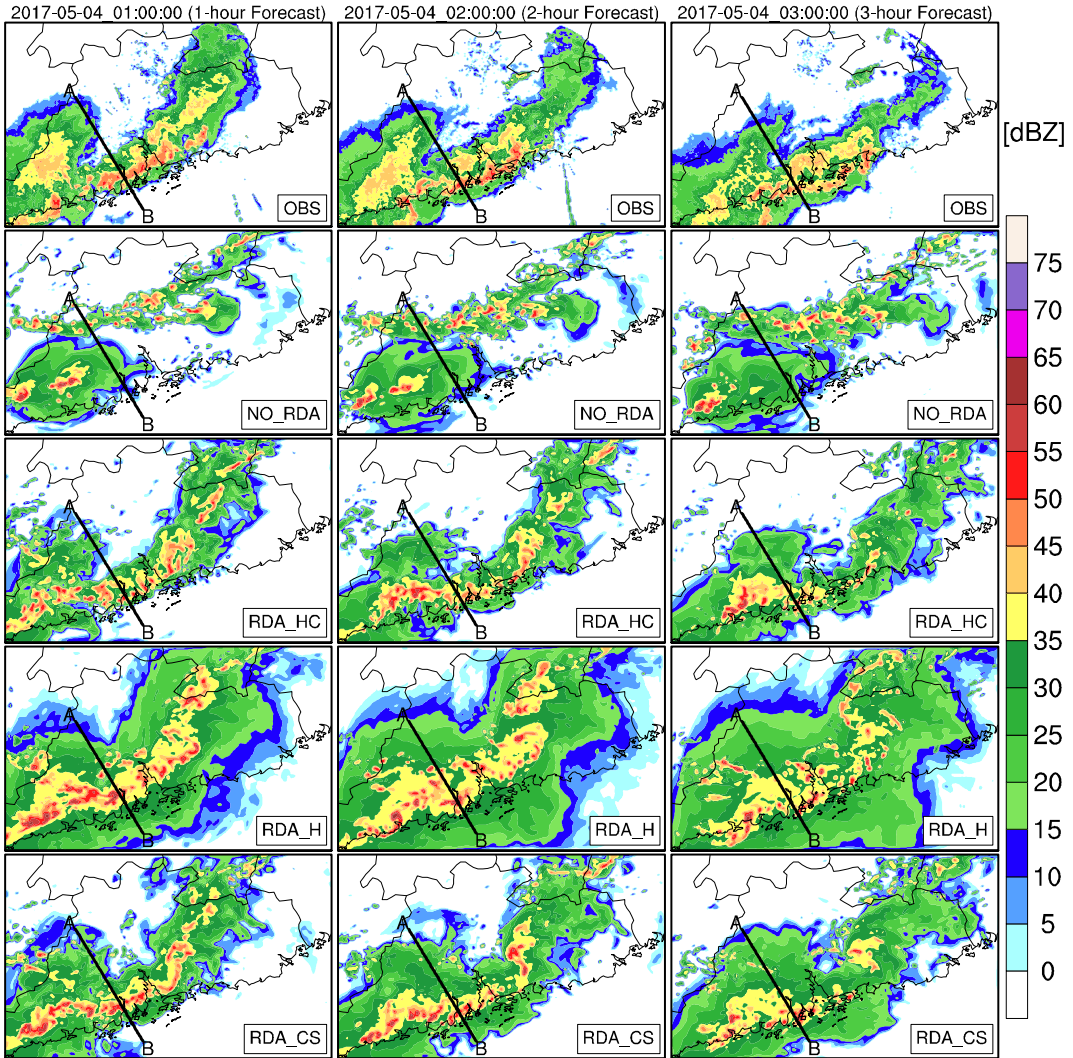


**Fig. 4.** Observed radar composite reflectivity (units: dBZ) at 0100–0300 UTC 04 May 2017 (1st row) and the corresponding 1–3-h composite reflectivity forecasts of the NO\_RDA (2nd row), RDA\_HC (3rd row), RDA\_H (4th row) and RDA\_CS (5th row), respectively. Thick solid lines in the panels (AB) denote the location of cross section in Fig. 5.

different values of the weighting coefficient  $w_2$  are applied to regions of convective and stratiform precipitations. The algorithm for convective and stratiform region segregation based on radar reflectivity is adopted from Zhang et al. (2008), which is used as an operational application algorithm at National Oceanic and Atmospheric Administration (NOAA). A grid column is defined as convective column if it meets one of the two following criteria: (1) Observed radar reflectivity factor at any height in the column is  $> 50$  dBZ; and (2) Observed radar reflectivity factor at or above the  $-10^\circ\text{C}$  height is  $> 30$  dBZ. All other columns with observed radar reflectivity  $> 20$  dBZ at any height in the column are classified as stratiform cloud columns. For each column, the layer limited by 25 dBZ from the bottom to the top is defined as a cloud layer. In RDA\_CS, the weighting coefficient ( $w_2$ ) is specified as

$$w_2 = \begin{cases} 1.0c, & \Delta Q_x > 0 \text{ and convective column and at cloud layer,} \\ & \text{or } \Delta Q_x < 0 \text{ and not at cloud layer;} \\ 0.8c, & \Delta Q_x > 0 \text{ and convective column and not at cloud layer,} \\ & \text{or stratiform column and at cloud layer;} \\ 0.6c, & \Delta Q_x > 0 \text{ and stratiform column and not at cloud layer,} \\ & \text{or } \Delta Q_x < 0 \text{ and convective column and at cloud layer;} \\ 1.0c, & \text{Others do not belong to above.} \end{cases}$$

where  $c = 1$  when  $\Delta Q_x > 0$ , and  $c = 0.5$  when  $\Delta Q_x < 0$ . The main

purpose of this heating scheme is to concentrate the radar data impact to strengthen the convective cloud development.

### 2.3. Evaluation method

A case study of the ten events is first evaluated through subjective analysis (Section 3) comparing the model simulated fields with the radar reflectivity and in-situ observational datasets from Meteorological Bureau of Shenzhen Municipality, China. Then objective statistical verification of all ten convection cases with multiple hourly forecast cycles are performed (presented in Section 4). The Fractions Skill Score (FSS), introduced by Roberts and Lean (2008), is employed to evaluate the forecast results. The formulation of FSS is,

$$\text{FSS} = 1 - \frac{\frac{1}{N} \sum_{i=1}^N (P_f - P_o)^2}{\frac{1}{N} \sum_{i=1}^N P_f^2 + \frac{1}{N} \sum_{i=1}^N P_o^2} = 1 - \frac{\sum_{i=1}^N (P_f - P_o)^2}{\sum_{i=1}^N P_f^2 + \sum_{i=1}^N P_o^2} \quad (4)$$

where  $N$  is the number of grid points in the domain, and  $P_f$  and  $P_o$  are the forecast and observed fraction of an elementary area, respectively. If FSS is 1.0, namely  $P_f$  is equal to  $P_o$ , it means that forecast is perfect. The FSS is one of fuzzy or neighborhood verification methods, which can properly display forecast skills dependent on different spatial scales for high-resolution precipitation forecasts. Mittermaier and Roberts

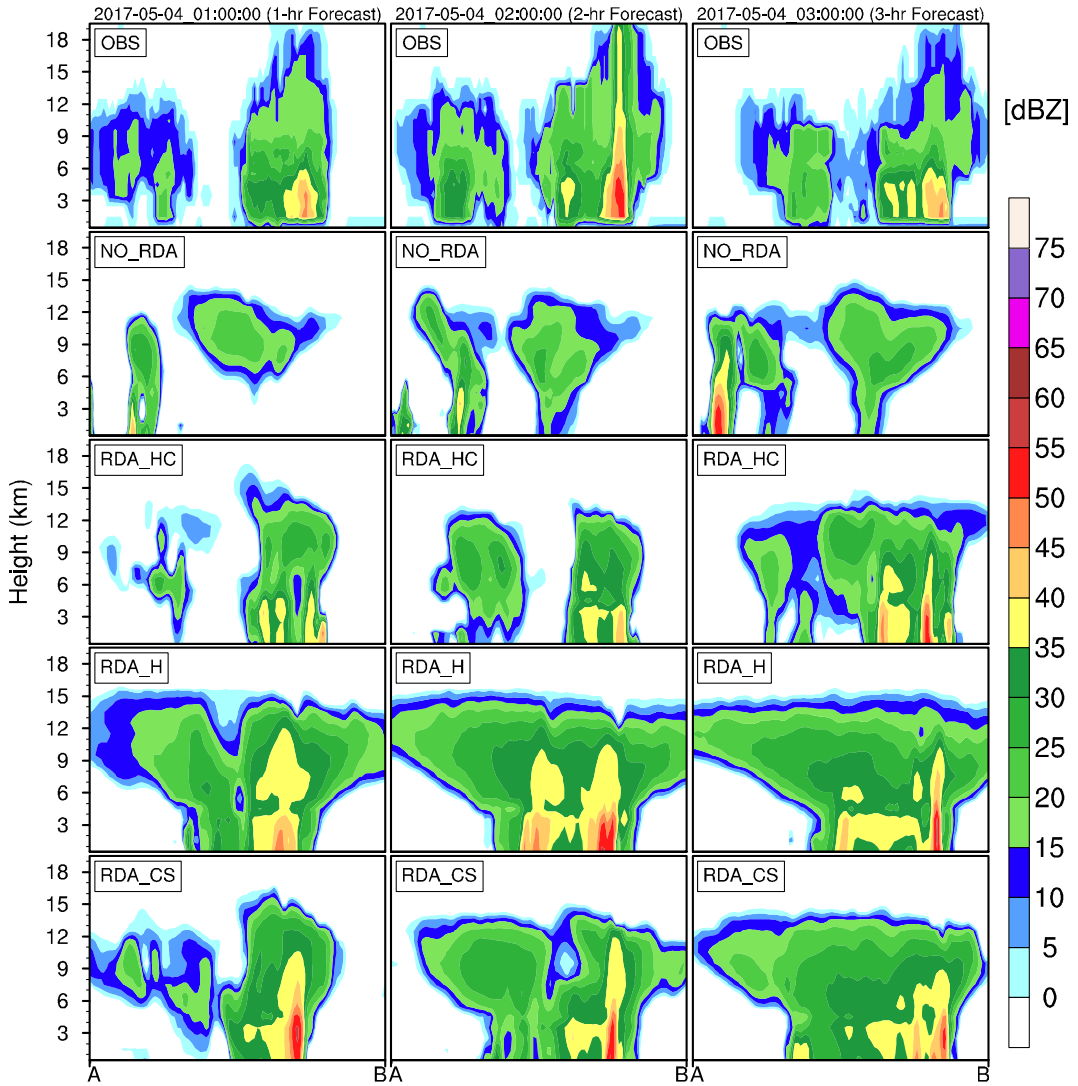


**Fig. 5.** Vertical cross sections of radar reflectivity (units: dBZ) from A to B (thick solid lines shown in Fig. 4) of observation (1st row), NO\_RDA (2nd row), RDA\_HC (3rd row), RDA\_H (4th row) and RDA\_CS (5th row) at 0100–0300 UTC 04 May 2017 from the 1st to 3rd column, respectively.

(2010)'s study shows that the FSS is a good measure of the spatial accuracy of precipitation forecasts.

### 3. Case study of 03–04 May 2017

In this section, detailed analyses of the experimental results for the event of 03–04 May 2017 (CASE02, Table 1) are presented, due to the better organization of squall line and more available observation data in this event than those of the other events. The forecast cycle selected here is with 6-h radar data nudging period (1800 UTC 03 May to 0000 UTC 04 May 2017) before the forecast started.

#### 3.1. Radar reflectivity

The composite reflectivity from multiple radar observations and 1–3-h model forecasts are shown in Fig. 4. Sun et al. (2014) demonstrated that RTFDDA-RDA can improve the hourly accumulated precipitation forecast in the first 12 h, however, we only focus on 0–3-h forecasts due to the small innermost domain (d03) and more statistical samples needed in this study. Here the model simulated reflectivity is computed using a diagnostic algorithm described in Stoelinga (2005). The observations reveal that in the local morning hours an intense convection band had developed along the southwest–northeast-

oriented coast of Guangdong Province and was moving southeast-ward (the 1st row panels of Fig. 4). The model forecasts without radar data assimilation (NO\_RDA, the 2nd row panels of Fig. 4) do not predict well-defined band structures near the coast, presenting larger forecast errors than the forecasts with RDA, which was also reported by Lompar et al. (2017, 2018). The forecasts from the three experiments with RDA, i.e., RDA\_HC, RDA\_H and RDA\_CS, all show improved skills in terms of echo patterns and intensity (panels in the 3rd–5th rows of Fig. 4). Among the three experiments with RDA, the intensity centers of the composite reflectivity in RDA\_HC forecasts (especially the 1-h forecast) appear less connected compared with those in the RDA\_H and RDA\_CS experiments. In the RDA\_H experiment where no cooling is applied during the nudging period, both the stratiform ( $> 15$  dBZ) and convective clouds ( $> 35$  dBZ) are broader. In the RDA\_CS forecasts, the stratiform cloud region is slightly wider than that in the observations, while the width of convective cloud region is similar to the observed. However, in all three experiments with RDA, the convective cloud region east of the Pearl River Estuary is not well predicted.

In order to examine the vertical structure of the storms, cross sections of radar reflectivity across the squall line (indicated by the thick solid lines from A to B in Fig. 4) are shown in Fig. 5. The model forecasts without RDA (NO\_RDA, the 2nd row panels of Fig. 5) do not capture the location of the strong convections ( $> 35$  dBZ), while the

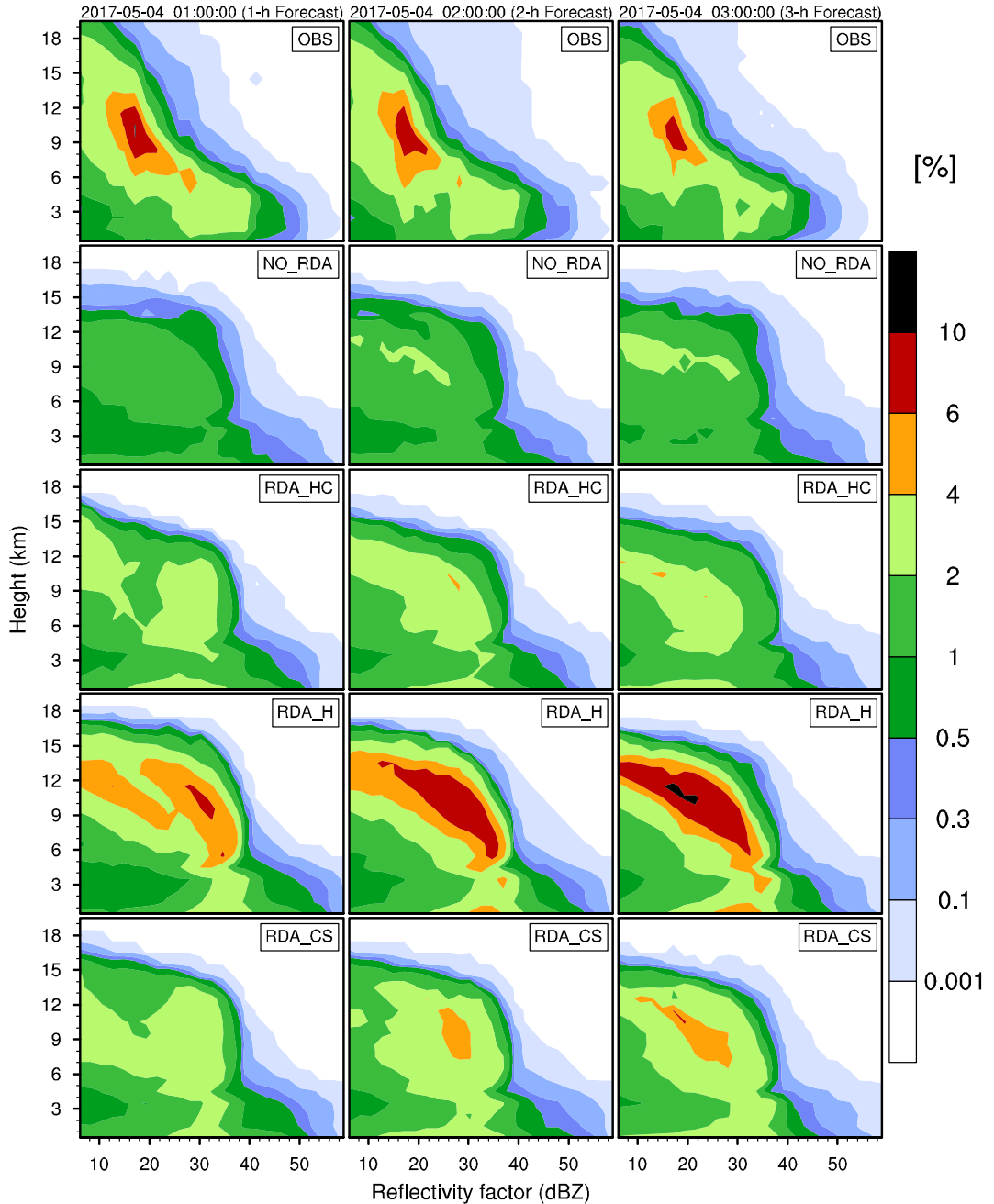


**Fig. 6.** Contoured frequency by altitude diagrams (CFADs) of radar reflectivity (units: dBZ) of observation (1st row), NO\_RDA (2nd row), RDA\_HC (3rd row), RDA\_H (4th row) and RDA\_CS (5th row) at 0100–0300 UTC 04 May 2017 from the 1st to 3rd column, respectively. Contour intervals are 0.001, 0.1, 0.3, 0.5, 1, 2, 4, 6, and 10%.

other forecasts with RDA (RDA\_HC, RDA\_H and RDA\_CS, panels in the 3rd–5th rows of Fig. 5) basically do. As the discrete distribution of strong composite reflectivity factor centers in the RDA\_HC experiment is shown in Fig. 4, the convection cores are discrete, and convective clouds of the RDA\_HC experiment is lower and weaker than the observed (the 3rd row panels of Fig. 5). In the RDA\_H experiment, stratiform and convective clouds are broader than those of observation and other experiments (the 4th row panels of Fig. 5). And the convective clouds in the RDA\_CS experiment are most similar to those of observation among all the model forecasts. However, the stratiform clouds are still a bit wider than observed clouds (the last row of Fig. 5).

Fig. 6 shows the contoured frequency by altitude diagrams (CFADs) of the observed and forecast radar reflectivity over the entire model domain. The CFADs was proposed by Yuter and Houze (1995) to reveal

statistical changes in vertical distributions of storm properties. From the CFADs of observed reflectivity (panels in the 1st row of Fig. 6), strong reflectivity is mainly located in the layer below 6 km where the reflectivity intensity is mostly over 30 dBZ. In contrast, in the upper level (above 6-km height), the observed radar reflectivity has a narrow distribution, and the dominant reflectivity intensity is around 20 dBZ. The model forecasts in the RDA\_H and RDA\_CS experiments resemble the observations in the lower level, but show broader distributions in the upper level. The overall magnitudes of the forecast reflectivity in RDA\_H and RDA\_CS (4th and 5th rows of Fig. 6) are larger than the observed. Especially, the frequency for 20–30-dBZ intensity is large in the RDA\_H experiment, indicating there is an over-forecast of spatial extent of reflectivity in this intensity range. And it is easy to understand that there is just heating but no cooling in this experiment, which is

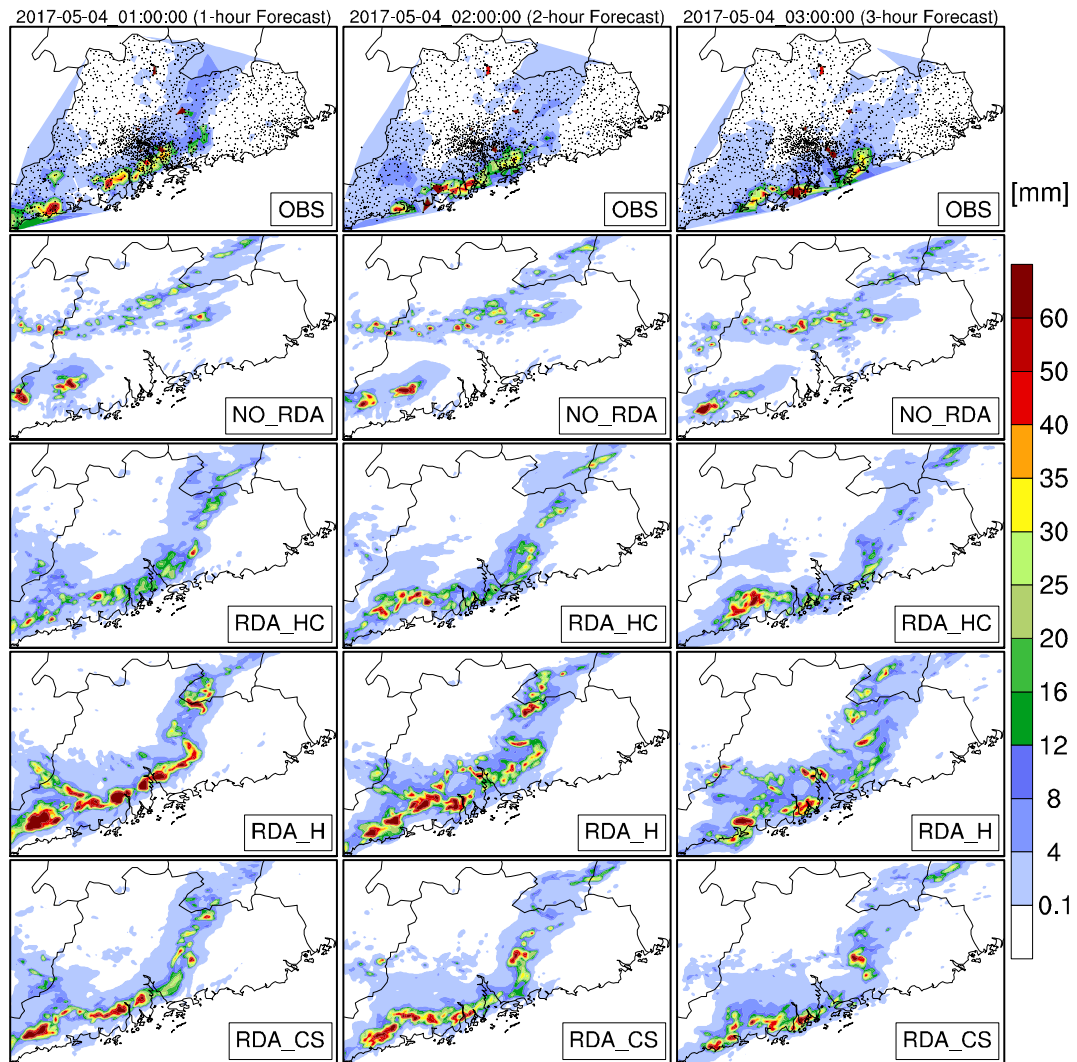


**Fig. 7.** 1-h accumulated precipitation (units: mm) of observation (1st row), NO\_RDA (2nd row), RDA\_HC (3rd row), RDA\_H (4th row) and RDA\_CS (5th row) at 0100–0300 UTC 04 May 2017 from the 1st to 3rd column, respectively. Small black dots in the panels of 1st row represent surface weather station locations.

more conducive to the development of cloud height and convective intensity. Besides, there is a big gap between the model forecasts of radar reflectivity distribution in the NO\_RDA and RDA\_HC experiments and the observed distribution (1st–3rd rows of Fig. 6).

Overall, the analysis of radar composite reflectivity, vertical cross sections, and CFADs of radar reflectivity shows that the model forecasts using convective-stratiform separated heating scheme are generally the best among all the model forecasts, in terms of reflectivity distribution and intensity.

### 3.2. Precipitation

The 1-h accumulated precipitation from observations and model forecasts from 0100 to 0300 UTC 04 May 2017 are shown in Fig. 7. Strong rain bands ( $> 12 \text{ mm}$ ) are mainly observed along the coast of Guangdong Province (panels in the 1st row of Fig. 7). The maximum 1-h observed accumulated precipitations all exceed 60 mm from 0100 to 0300 UTC. All the experiments except NO\_RDA capture the main heavy rain bands along the coast of Guangdong Province (Fig. 7). The precipitation intensity in the RDA\_HC experiment is weaker than the observed, while the forecast precipitation of the RDA\_H experiment is stronger than the observed precipitation (panels in the 3rd–4th rows of Fig. 7). There are more strong precipitation centers in the RDA\_H experiment than the observed, especially in the area to the northeast of

the Pearl River Estuary (panels in the 4th rows of Fig. 7). Though some differences exist between the observed precipitation and forecast precipitation in the RDA\_CS experiment, precipitation in the RDA\_CS experiment resembles the observed precipitation, in terms of its distribution and intensity, especially in the west of the Pearl River Estuary (panels in the last row of Fig. 7).

In order to understand the radar data impact on the model wind and thermodynamic fields, the observed and forecast air temperatures at 2-m level, wind vectors at 850-hPa level and geopotential height at 500-hPa level are shown in Fig. 8. Since sounding data during 0100–0300 UTC 04 May 2017 are not available, the observed wind fields and geopotential height fields shown in the 1st row panels of Fig. 8 are plotted using the sounding data at 0000 UTC 04 May 2017. The observed 850-hPa wind directions over the coastal areas are mainly southwesterly along the coast of Guangdong Province, and all the model forecasts show similar wind directions over these areas. And in observation (the 1st row panels of Fig. 8), northwesterly and southwesterly winds are dominant on the northwest and northeast regions of the Pearl River Estuary, respectively. Therefore, the wind convergence is mainly located along the coast, where the main precipitation locates, especially in the region to the west of the Pearl River Estuary. The NO\_RDA experiment produces southwesterly winds basically in the most part of Guangdong Province (panels in the 2nd row of Fig. 8), and that is why the model did not capture the main rain bands in the

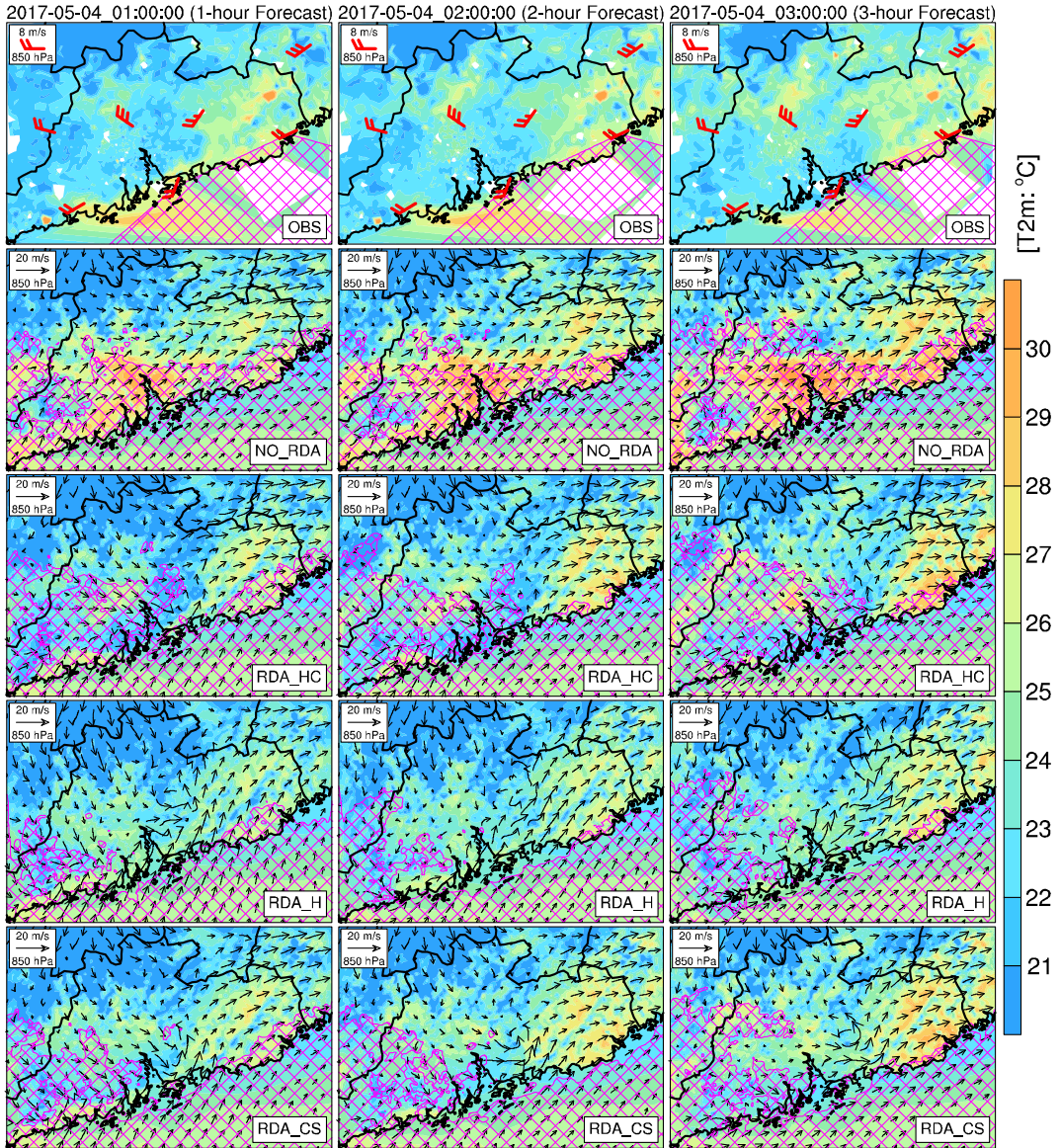


**Fig. 8.** Air temperature at 2-m level (shaded, units: °C), wind vectors at 850-hPa level (units:  $m s^{-1}$ ), areas whose 500-hPa geopotential height are larger 5880 gpm (diamond fill pattern). In observation (1st row), air temperature fields (shaded) are at 0100–0300 UTC 04 May 2017, respectively, and all wind bars at 850-hPa and geopotential height fields are at 0000 UTC 04 May 2017. In the forecast experiments, NO\_RDA (2nd row), RDA\_HC (3rd row), RDA\_H (4th row) and RDA\_CS (5th row), all fields are at 0100–0300 UTC 04 May 2017 from the 1st to 3rd column, respectively.

NO\_RDA experiment. The wind fields of the model forecasts with RDA, especially in the RDA\_CS experiment, generally resemble the observed wind fields (panels in the 3rd–5th rows of Fig. 8).

Also noteworthy is that the northern edge of the subtropical high (areas where 500-hPa geopotential height are over 5880 gpm) in the observation is located along the coast of Guangdong Province (panels in the 1st row of Fig. 8). The northern edge of the subtropical high in the NO\_RDA experiment is further north, while it is located near the coast in the model forecasts with RDA, especially in the RDA\_CS experiment (Fig. 8), which is the main factor affecting the location of rain bands. Besides, because the precipitation distributions in the experiments with RDA are similar to that of observation, the locations of cold pools also resemble the observed cold pool locations, especially in the RDA\_CS experiment. However, the cold pools in the NO\_RDA experiment are very different from those of observation (Fig. 8).

Overall, the case study demonstrates that the radar data nudging schemes, especially the one using convective-stratiform separated heating algorithm, are capable of analyzing convective storm mesoscale

and convective-scale features in a good accuracy and significantly improve the short-term precipitation forecast of the convective storm.

#### 4. Statistical verification results

In this section, Fractions Skill Score (FSS) is firstly computed for CASE02 to evaluate all 1–3-h forecasts in the CASE02 with hourly forecast cycles objectively, and then statistical verification scores over all ten convection cases with hourly forecast cycles are presented.

Fig. 9 shows the FSSs of all 1–3-h composite reflectivity forecasts at 35-dBZ threshold and 60-km (30-km radius) horizontal scale in CASE02. It is obvious that, the FSSs of the forecasts with RDA (RDA\_HC, RDA\_H and RDA\_CS, whose averaged FSSs are all  $> 0.58$ ) are apparently higher compared to the FSSs of the forecasts without RDA (NO\_RDA, whose averaged FSSs are  $< 0.26$ ) for the 1–3-h forecasts (Figs. 9a–c). Among the FSSs of the forecasts with RDA (RDA\_HC, RDA\_H and RDA\_CS), none always has the highest FSSs. On average, the FSSs of RDA\_CS are the highest in the 1-h (0.795) and 2-h (0.688)

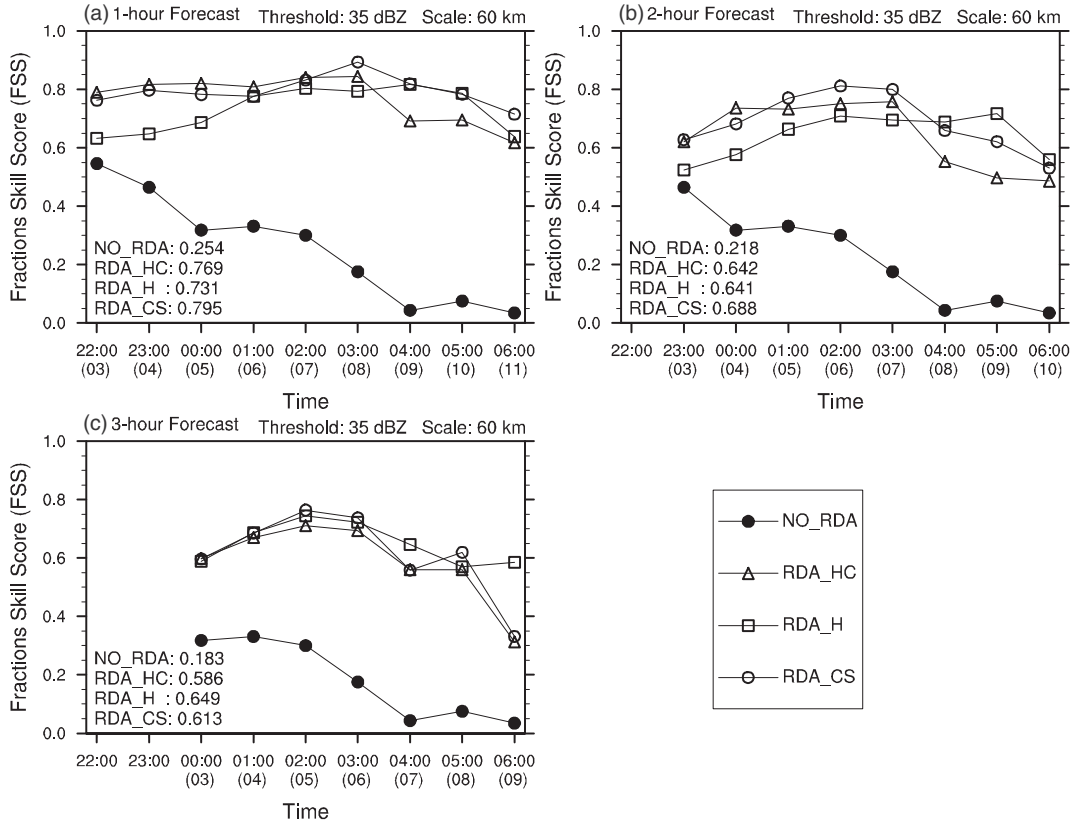


**Fig. 9.** Fractions skill scores (FSSs) of all 1–3-h composite reflectivity forecasts at 35-dBZ threshold and 60-km (30-km radius) horizontal scale in CASE02. Averaged FSSs in the 1–3-h forecasts are shown in the bottom-left regions of each panel. The numbers inside brackets below the time axis represent radar data nudging periods.

forecasts, while it ranks second (0.613) in the 3-h forecast, which is slightly lower than that of RDA\_H (0.649) (Fig. 9). In general, the forecasts with convective-stratiform separated heating scheme outperforms those of the other two experiments in this case.

The numerical experiments described in in Table 2 have been carried out for the ten severe convection cases (Table 1) and FSSs are computed over all the cases. The box-and-whisker plots shown in Fig. 10 give the spread of FSSs of all 1–3-h composite reflectivity forecasts of the ten severe convective storms at 25-, 35- and 45-dBZ thresholds and 60-km (30-km radius) horizontal scale. There are a total of 90, 80 and 70 samples for the 1-, 2-, and 3-h forecasts, respectively. The ends of the whiskers indicate the minimal and maximal values of the scores. The lower and upper limits of the box correspond to the 25th and 75th percentiles, and the point and dividing line within the box are the mean and median scores, respectively. At the 25-dBZ threshold, the averaged FSSs of RDA\_CS are the highest except for the 1-h forecasts (Fig. 10a). For the 1-h forecasts, the RDA\_CS skill is slightly lower than that of RDA\_HC, with a small difference between 0.872 in RDA\_CS and 0.879 in RDA\_HC. The analysis of Section 3.1 has pointed out that the RDA\_CS forecasts produce broader stratiform cloud region, which may be the reason why the FSS of RDA\_CS is slightly lower than that of RDA\_HC at the 25-dBZ threshold in the 1-h forecast. Moreover, the height of the boxes between the 25th and 75th percentiles in the RDA\_CS experiment are smaller compared with those of the other experiments, especially NO\_RDA (Fig. 10a). It indicates that the FSS of RDA\_CS is relatively stable. And as for the FSSs at 35- and 45-dBZ thresholds, the averaged FSSs of RDA\_CS are the highest among all the 1–3-h forecasts (Figs. 10b and c). Besides, the FSSs of RDA\_HC are mostly higher than those of RDA\_H, indicating that latent-heat cooling effect during the nudging period should not be neglected. Based on the FSSs for the hourly forecast cycles with ten convective cases, the model forecasts with the RDA are all much better than those without RDA, and

the performance of forecasts with the refined convective-stratiform separated heating scheme outperforms the experiments with bulk latent heating/cooling or heating only approaches.

## 5. Discussions

The subjective and statistical verification of the extensive modeling experiments with RTFDDA-RDA in the last two sections shows that RTFDDA-RDA is able to significantly improve the short-term precipitation forecasting of the convective storms through nudging cloud hydrometeors retrieved from radar reflectivity and the associated latent heat release. Nevertheless, there are many rooms for future improvements. An assumption in the original RTFDDA-RDA scheme is that the latent heat innovation is proportional to the radar reflectivity innovation, i.e. the differences between the observed and simulated radar reflectivity. As a matter of fact, radar reflectivity only reflects an instantaneous sum effect of precipitation particles (rain water, snow and graupel) at grid boxes. These precipitation particles were produced by complex microphysical processes (condensation/deposition, evaporation sublimation, accretion, breaking, etc. of cloud/precipitation particles) and affected by dynamical advection and diffusion processes (Ćurić and Janc, 1987). The exact location and time of the latent heat release are affected by these microphysical and dynamical processes, and thus there is not a one-to-one correspondence between the reflectivity-derived precipitation particles (rain water, snow and graupel) at a grid box and the latent heat release occurred at this grid. Our results show that model performance is improved when a convective-stratiform separated latent-heating scheme is applied. Earlier works divide a convective storm into the two basic types of cloud and precipitation regions, convective and stratiform precipitation respectively (e.g. Houze, 2014). Convective regions are always associated with strong vertical motion throughout the troposphere, while stratiform

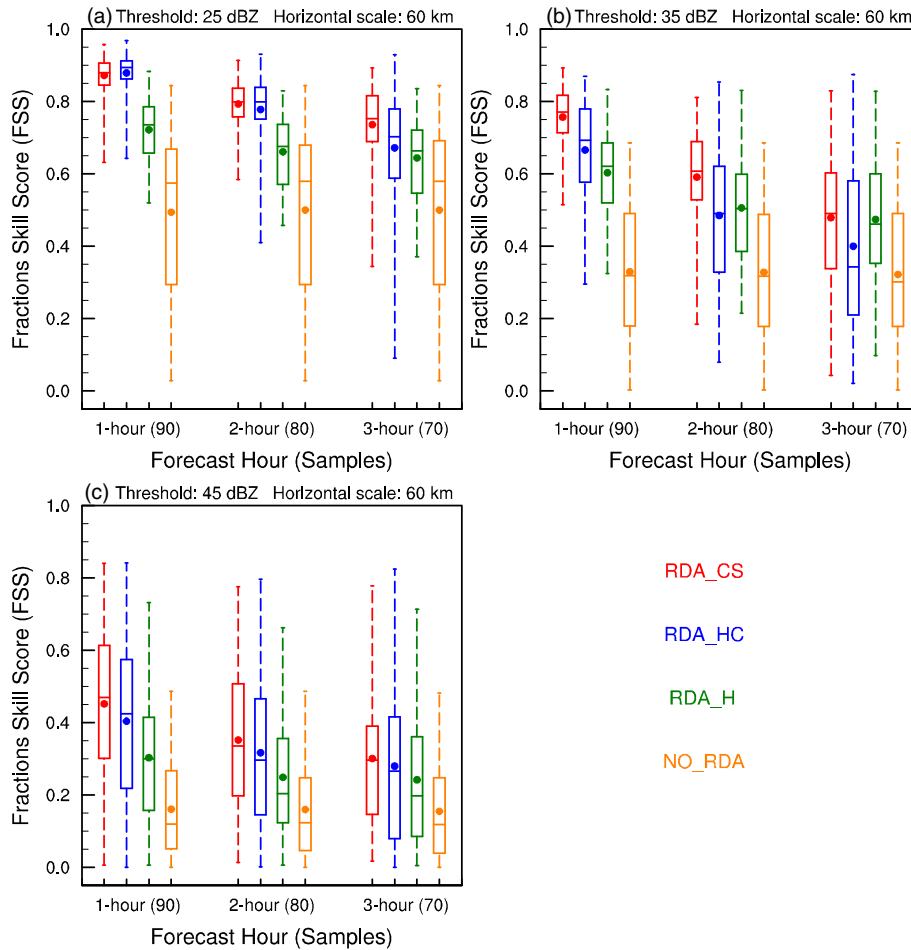


**Fig. 10.** Box-and-whisker plots of Fractions skill scores (FSSs) of all 1–3-h forecasts of composite reflectivity for the ten severe convective storms at 25-dBZ (a), 35-dBZ (b) and 45-dBZ (c) thresholds and 60-km (30-km radius) horizontal scale. The extremes of the whiskers indicate the largest and smallest FSSs, the lower and upper limits of the boxes correspond to the 25th and 75th percentiles, the dividing line represents the median value, and the points represent the average value. Red: RDA\_CS, blue: RDA\_HC, green: RDA\_H, and orange: NO\_RDA. The numbers inside brackets below the horizontal axis represent the number of samples. (For interpretation of the references to color in this figure legend, the reader is referred to the web version of this article.)

regions are characterized by a relatively uniform weak ascending or descending motion (Xu, 1995; Sui et al., 2007; Ahmed and Schumacher, 2015). Many studies have shown that cloud microphysical processes are distinctly different in convective and stratiform regions (e.g. Steiner et al., 1995; Morrison et al., 2009; Luo et al., 2010; Feng et al., 2011; Penide et al., 2013; Wu et al. 2013; Houze, 2014; Thurai et al., 2016), and dramatically different latent heating distributions in the convective and stratiform regions (Houze, 1982; Xu, 1995; Yang and Smith, 2000). Tao et al. (2001, 2010) developed convective-stratiform heating algorithms to estimate heating profiles and temporal evolution of the cloud latent heating structures. Therefore, applying differentiated latent heating rates in convective and stratiform regions can be considered as an initial step to tackle the aforementioned issue of hydrometeors and latent heat release inconsistency, and in future it is important to improve the latent heating algorithm for more accurate simulation of the timing, location and amount of the latent heat release.

Besides the uncertainties in determining latent heat release from radar reflectivity measurements, the assumptions and empirical parameters in the relationships of hydrometeor variables and the observed radar reflectivity (Rasmussen et al., 2003), microphysical parameterizations (Thompson et al., 2008), and the nudging parameters' specification (weighting coefficient  $w_1$  and  $w_2$ ) also affects the performance of radar data assimilation. To illustrate the impact of these uncertainties, Fig. 11 shows observed and model radar composite reflectivity factor (Figs. 11a1–b3), and their difference (Figs. 11c1–c3) for the RDA\_CS experiment of CASE02 with 6-h radar data nudging period (1800 UTC 03 May–0000 UTC 04 May 2017) during the data assimilation period. The composite reflectivity in RDA\_CS experiment resembles the observation, in terms of its intensity and distribution pattern of the squall line system (Figs. 11a1–b3). At the 2nd hour of radar

data nudging (at 2000 UTC 03 May), the observed composite reflectivity was larger than that of RDA\_CS experiment over the most cloud regions (Fig. 11c1).

From the cross section of the hydrometeor mixing ratio difference between the radar retrieved and the model simulation, it can be seen that the observed total hydrometeor content was higher in the lower troposphere and lower in the upper troposphere than those in the model (Fig. 11d1). As a result, latent heat was mainly added in the lower troposphere (Fig. 11e1), which stimulated and supported the development of convection. By the 4th hour of radar data nudging (2200 UTC 03 May), two zones in the composite reflectivity difference (Fig. 11c2) can be found, one is positive (the observation is larger than the model) and the other is negative (the observation is less than the model). This is because the observed squall line was moving slightly faster than that of the model (Figs. 11c2 and d2). Consequently, the latent heating (cooling) regions were mainly in front (rear) of the squall line, respectively (Fig. 11e2). At the end of the 6-h radar data nudging window (0000 UTC 04 May), the locations of the observed and model squall lines were close to each other, especially within the boxes shown in Fig. 11c3. However, there are still some differences in the vertical structure of hydrometeors (Fig. 11d3), leading to a certain amount of latent heat nudged (Fig. 11e3).

These results show that it remains a challenging work to retrieve and replicate the complex microphysical, thermodynamic and dynamical structures and processes of severe convection with radar data assimilation. Besides the large uncertainty in the relationships between the observed radar reflectivity and the hydrometeors in the cloud, the model hydrometeor "climatology" of a microphysical scheme can differ significantly from those in nature clouds. These differences can result in persistent artificial imbalance between the nudged hydrometeors and

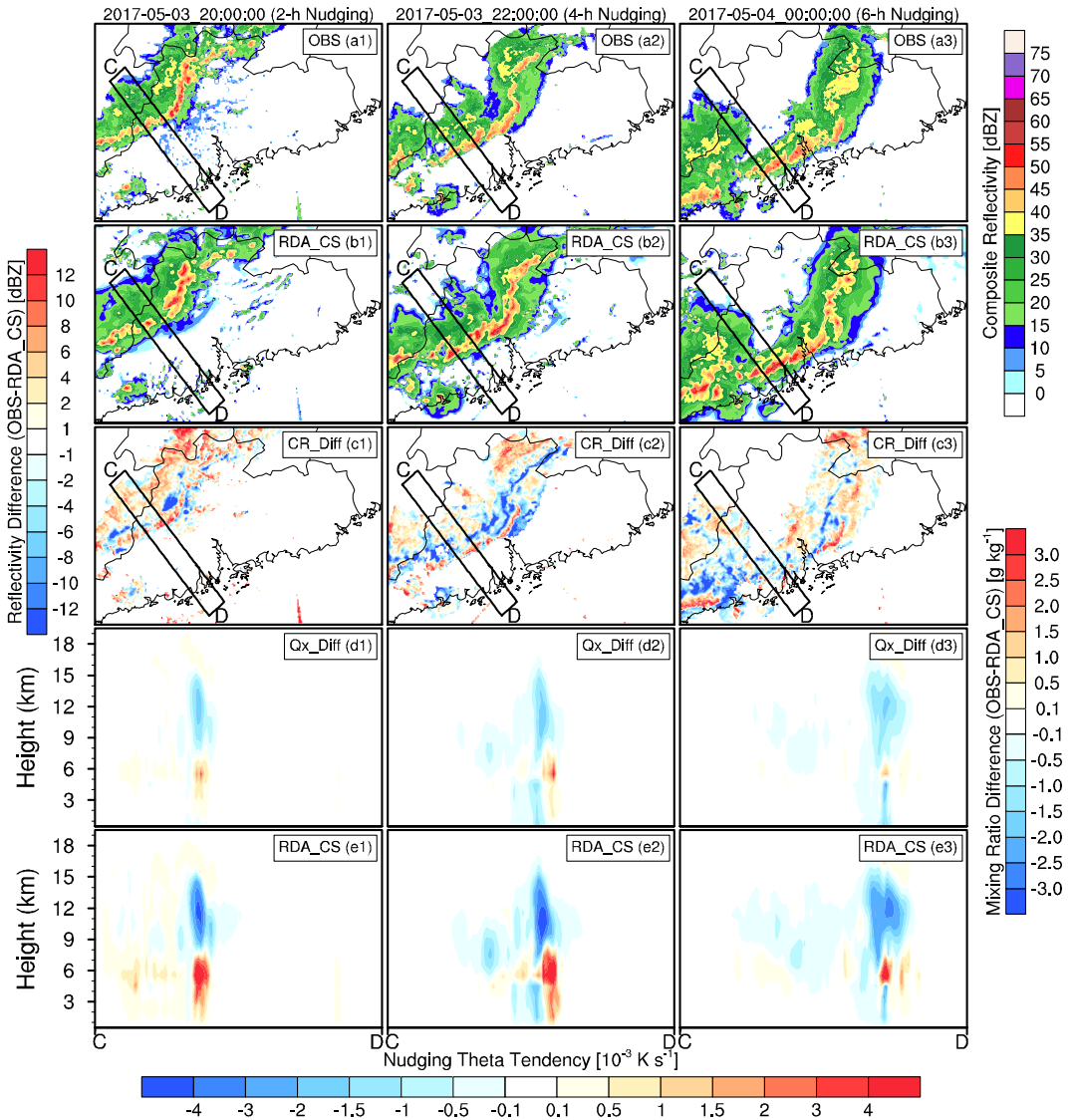


**Fig. 11.** Observed (OBS, a1–a3) and model (RDA\_CS experiment, b1–b3) radar composite reflectivity (units: dBZ), and their difference (OBS – RDA\_CS, c1–c3) at 2000 UTC 03 May 2017 (a1, b1, c1), 2200 UTC 03 May 2017 (a2, b2, c2) and 0000 UTC 04 May 2017 (a3, b3, c3), respectively; Cross sections of the difference between total radar retrieved ( $Q_r + Q_s$ ) and model (for RDA\_CS,  $Q_r + Q_s + Q_g$ ) hydrometeor mixing ratio (d1–d3, units:  $\text{g kg}^{-1}$ ); and the potential temperature tendency (e1–e3, units:  $10^{-3} \text{ K s}^{-1}$ ) due to latent heat nudging in RDA\_CS. The locations of the cross-sections for d1–e1, d2–e2 and d3–e3 are from C to D, and the values are averaged perpendicular to CD within the boxes shown in a1, b1 and c1 (2000 UTC 03 May 2017), a2, b2 and c2 (2200 UTC 03 May 2017), and a3, b3 and c3 (0000 UTC 04 May 2017), respectively. The color bar on the left side is for c1–c3, the color bars on the right side are for a1–b3 (top) and d1–d3 (bottom), respectively, and the color bar on the bottom is for e1–e3.

the hydrometeors that a microphysical scheme sustains. For example, in the current experiment, the retrieved hydrometeor content was mostly less than that of the model simulation in the upper troposphere (Figs. 11d1–d3), which led to continuously unrealistic drying and cooling by nudging, even after 6 h of the RDA processes. Future works should be conducted toward improving the accuracy of the relationships of observed radar reflectivity and hydrometeors (e.g. with dual-polarization radar measurements), microphysical processes (e.g., graupel growth through riming, ice crystal to snow conversion, snow's terminal velocity, etc. Thompson et al., 2008), spatiotemporal difference between latent heat release and reflectivity growth, and nudging coefficients. Besides radar data assimilation method, better micro-physics scheme and more appropriate initial conditions also are very important to the precipitation forecasting improvement (Ćurić and Janc, 2011a, 2011b).

## 6. Conclusions

In this study, the NCAR WRF-based real-time four-dimensional data assimilation and short-term forecasting system, enhanced with radar data assimilation, RTFDDA-RDA, was evaluated for the short-term (mainly 0–3 h) precipitation forecasts of severe convective storms. The system employed an analysis nudging (Newtonian relaxation) technique for assimilating radar reflectivity data into the WRF model. Hydrometeors and latent heat, retrieved from radar reflectivity are nudged into the WRF hydrometeor and thermodynamic equations, termed as the hydrometeor and latent heat nudging (HLHN) scheme. A RTFDDA-RDA system has been running for an operational rapid-update forecasting in the Meteorological Bureau of Shenzhen Municipality, China. Recently, a new latent heating scheme, convective-stratiform separated heating scheme, has been developed in RTFDDA-RDA. The system was run to produce hindcasts for ten severe convective storms occurred in the Guangdong region during the 2017 rainy season. The

radar data assimilation impact was analyzed through subjective verification of a case study and statistical verification of hourly forecast cycles for ten convective storms. The major results can be summarized as follows,

- (1) By nudging cloud hydrometeors retrieved from radar reflectivity and the corresponding latent heat, the RTFDDA-RDA system is capable of analyzing mesoscale and convective-scale features in a good accuracy and it leads to significantly improve short-term precipitation forecasting of convective storms.
- (2) Subjective analyses of a case study demonstrate that RTFDDA-RDA is capable of forecasting the locations and structures of convective storms with good accuracy. The statistical FSSs of nine hourly forecast cycles for ten severe convective storms show 130%, 80% and 49% improvements of the RDA\_CS than the NO\_RDA runs at 35-dBZ threshold and 60-km (30-km radius) horizontal scale, for 1-, 2- and 3-h forecasts, respectively.
- (3) The sensitivity experiments with three different latent heating algorithms show that the newly introduced latent heating scheme, convective-stratiform separated heating scheme, outperforms the original single heating scheme.

We pointed out that even though the convective-stratiform separated heating scheme forecasted the convective storms pretty accurately, it produced broader stratiform cloud regions than the observation. We also found that the empirical latent-heating nudging coefficient is sensitive. More studies should be conducted to understand and optimize its effect. This can be done with controlled experiments with observing system simulation experiments (OSSEs). Furthermore, there are only ten cases included in this study. More case studies and long-term real-time operation evaluation should be taken to generalize the conclusions. In addition, intercomparison of different assimilation approaches (e.g., RTFDDA-RDA, 4DVAR and EnKF) will be conducted for same convective cases at the same region in future. We also wanted to note that RTFDDA-RDA modifies cloud dynamics mainly through the thermodynamic feedback of the hydrometer and latent heat nudging processes. In future, three-dimensional wind fields retrieved from radar radial winds should be assimilated into the model to further improve the forecast of convection. Finally, with the development of dual-polarization radars, RTFDDA-RDA with improved hydrometeor classification shall be studied.

## Acknowledgements

This work was partially supported by the State Grid Corporation of China under the Sciences and Technology Project: SGTYHT/14-JS-188. The authors thank Mr. Wenhui Zhang of the Meteorological Bureau of Shenzhen Municipality, Shenzhen, China for providing the radar and rain gauge data used in this study. The authors are also grateful to Dr. Yonghui Wu of Panasonic Weather Solutions for his contribution to RTFDDA-RDA code development, and very appreciate of Dr. Matthias Steiner (NCAR) and the two anonymous reviewers for their useful suggestions and comments. The authors would like to acknowledge high-performance computing support from Yellowstone (ark:/85065/d7wd3xhc) provided by NCAR's Computational and Information Systems Laboratory. NCAR is sponsored by the National Science Foundation.

## References

- Ahmed, F., Schumacher, C., 2015. Convective and stratiform components of the precipitation-moisture relationship. *Geophys. Res. Lett.* 42, 10453–410462.
- Benjamin, S., et al., 2016. A north American hourly assimilation and model forecast cycle: the rapid refresh. *Mon. Weather Rev.* 144, 1669–1694.
- Bytheway, J., Kummerow, C., Alexander, C., 2017. A features-based assessment of the evolution of warm season precipitation forecasts from the HRRR model over three years of development. *Weather Forecast.* 32, 1841–1856.
- Ćurić, M., Janc, D., 1987. On the influence of entrainment and forced lifting on some products of a 1-D model of a Cb cloud. *Atmos. Res.* 21, 151–169.
- Ćurić, M., Janc, D., 2011a. Analysis of predicted and observed accumulated convective precipitation in the area with frequent split storms. *Hydrol. Earth Syst. Sci.* 15, 3651–3658.
- Ćurić, M., Janc, D., 2011b. Comparison of modeled and observed accumulated convective precipitation in mountainous and flat land areas. *J. Hydrometeorol.* 12, 245–261.
- Dowell, D.C., Wicker, L.J., Snyder, C., 2011. Ensemble Kalman filter assimilation of radar observations of the 8 May 2003 Oklahoma City Supercell: influences of reflectivity observations on storm-scale analyses. *Mon. Weather Rev.* 139, 272–294.
- Feng, Z., Dong, X., Xi, B., Schumacher, C., Minnis, P., Khaiyer, M., 2011. Top-of-atmosphere radiation budget of convective core/stratiform rain and anvil clouds from deep convective systems. *J. Geophys. Res. Atmos.* 116, D23202. <http://dx.doi.org/10.1029/2011JD016451>.
- Gao, J., Stensrud, D.J., 2012. Assimilation of reflectivity data in a convective-scale, cycled 3DVAR framework with hydrometeor classification. *J. Atmos. Sci.* 69, 1054–1065.
- Grell, G.A., Freitas, S.R., 2014. A scale and aerosol aware stochastic convective parameterization for weather and air quality modeling. *Atmos. Chem. Phys.* 14, 5233–5250.
- Haase, G., Crewell, S., Simmer, C., Wergen, W., 2000. Assimilation of radar data in mesoscale models: physical initialization and latent heat nudging. *Phys. Chem. Earth B Hydrol. Oceans Atmos.* 25, 1237–1242.
- Hong, S.-Y., Noh, Y., Dudhia, J., 2006. A new vertical diffusion package with an explicit treatment of entrainment processes. *Mon. Weather Rev.* 134, 2318–2341.
- Houze, R.A., 1982. Cloud clusters and large-scale vertical motions in the tropics. *J. Meteorol. Soc. Japan.* 60, 396–410.
- Houze, R.A., 2014. *Cloud Dynamics, Second Edition*. Academic Press.
- Iacono, M.J., Delamere, J.S., Mlawer, E.J., Shephard, M.W., Clough, S.A., Collins, W.D., 2008. Radiative forcing by long-lived greenhouse gases: calculations with the AER radiative transfer models. *J. Geophys. Res. Atmos.* 113, D13103. <http://dx.doi.org/10.1029/2008JD009944>.
- Korsholm, U.S., Petersen, C., Sass, B.H., Nielsen, N.W., Jensen, D.G., Olsen, B.T., Gill, R., Vedel, H., 2015. A new approach for assimilation of 2D radar precipitation in a high-resolution NWP model. *Meteorol. Appl.* 22, 48–59.
- Liu, Y., et al., 2008a. The operational mesogamma-scale analysis and forecast system of the US Army Test and Evaluation Command. Part I: overview of the modeling system, the forecast products, and how the products are used. *J. Appl. Meteorol. Climatol.* 47, 1077–1092.
- Liu, Y., et al., 2008b. The operational mesogamma-scale analysis and forecast system of the US Army test and evaluation command. Part II: interrane comparison of the accuracy of model analyses and forecasts. *J. Appl. Meteorol. Climatol.* 47, 1093–1104.
- Lompar, M., Ćurić, M., Romanic, D., 2017. Simulation of a severe convective storm using a numerical model with explicitly incorporated aerosols. *Atmos. Res.* 194, 164–177.
- Lompar, M., Ćurić, M., Romanic, D., 2018. Implementation of a gust front head collapse scheme in the WRF numerical model. *Atmos. Res.* 203, 231–245.
- Luo, Y., Wang, Y., Wang, H., Zheng, Y., Morrison, H., 2010. Modeling convective-stratiform precipitation processes on a Mei-Yu front with the weather research and forecasting model: comparison with observations and sensitivity to cloud microphysics parameterizations. *J. Geophys. Res. Atmos.* 115, D18117. <http://dx.doi.org/10.1029/2010jd013873>.
- Min, K.H., Choo, S., Lee, D., Lee, G., 2015. Evaluation of WRF cloud microphysics schemes using radar observations. *Weather Forecast.* 30, 1571–1589.
- Mittermaier, M., Roberts, N., 2010. Intercomparison of spatial forecast verification methods: identifying skillful spatial scales using the fractions skill score. *Weather Forecast.* 25, 343–354.
- Morrison, H., Thompson, G., Tatarskii, V., 2009. Impact of cloud microphysics on the development of trailing stratiform precipitation in a simulated squall line: comparison of one- and two-moment schemes. *Mon. Weather Rev.* 137, 991–1007.
- Penide, G., Kumar, V.V., Protat, A., May, P.T., 2013. Statistics of drop size distribution parameters and rain rates for stratiform and convective precipitation during the north Australian wet season. *Mon. Weather Rev.* 141, 3222–3237.
- Rasmussen, R., Dixon, M., Vasiloff, S., Hage, F., Knight, S., Vivekanandan, J., Xu, M., 2003. Snow nowcasting using a real-time correlation of radar reflectivity with snow gauge accumulation. *J. Appl. Meteorol.* 42, 20–36.
- Roberts, N.M., Lean, H.W., 2008. Scale-selective verification of rainfall accumulations from high-resolution forecasts of convective events. *Mon. Weather Rev.* 136, 78–97.
- Snyder, C., Zhang, F., 2003. Assimilation of simulated Doppler radar observations with an ensemble Kalman filter. *Mon. Weather Rev.* 131, 1663–1677.
- Steiner, M., Houze, R.A., Yuter, S.E., 1995. Climatological characterization of three-dimensional storm structure from operational radar and rain gauge data. *J. Appl. Meteorol.* 34, 1978–2007.
- Stephan, K., Klink, S., Schraff, C., 2008. Assimilation of radar-derived rain rates into the convective-scale model COSMO-DE at DWD. *Q. J. R. Meteorol. Soc.* 134, 1315–1326.
- Stoelinga, M.T., 2005. Simulated equivalent reflectivity factor as currently formulated in RIP: Description and possible improvements. In: Read/Interpolate/Plot Implementation Document, 5 pp. Available online at: <http://citeseerx.ist.psu.edu/viewdoc/download?doi=10.1.1.522.925&rep=rep1&type=pdf>.
- Sugimoto, S., Crook, N.A., Sun, J., Xiao, Q., Barker, D.M., 2009. An examination of WRF 3DVAR radar data assimilation on its capability in retrieving unobserved variables and forecasting precipitation through observing system simulation experiments. *Mon. Weather Rev.* 137, 4011–4029.
- Sui, C.H., Tsay, C.T., Li, X.F., 2007. Convective - stratiform rainfall separation by cloud content. *J. Geophys. Res. Atmos.* 112, D14213. <http://dx.doi.org/10.1029/2006jd008082>.
- Sun, J., 2005. Initialization and numerical forecasting of a supercell storm observed

- during STEPS. *Mon. Weather Rev.* 133, 793–813.
- Sun, J., Crook, N.A., 1997. Dynamical and microphysical retrieval from Doppler radar observations using a cloud model and its adjoint. Part I: model development and simulated data experiments. *J. Atmos. Sci.* 54, 1642–1661.
- Sun, J., Wang, H., 2013. Radar data assimilation with WRF 4D-Var. part II: comparison with 3D-Var for a squall line over the U.S. Great Plains. *Mon. Weather Rev.* 141, 2245–2264.
- Sun, J., et al., 2014. Use of NWP for nowcasting convective precipitation: recent progress and challenges. *Bull. Am. Meteorol. Soc.* 95, 409–426.
- Tao, W.-K., et al., 2001. Retrieved vertical profiles of latent heat release using TRMM rainfall products for February 1998. *J. Appl. Meteorol.* 40, 957–982.
- Tao, W.-K., Lang, S., Zeng, X., Shige, S., Takayabu, Y., 2010. Relating convective and stratiform rain to latent heating. *J. Clim.* 23, 1874–1893.
- Tewari, M., et al., 2004. Implementation and verification of the unified Noah land surface model in the WRF model. In: 20th Conf. on Weather Analysis and Forecasting/16th Conf. on Numerical Weather Prediction, Seattle, WA. Amer. Meteorol. Soc 14.2a. Available online at: [https://ams.confex.com/ams/84Annual/techprogram/paper\\_69061.htm](https://ams.confex.com/ams/84Annual/techprogram/paper_69061.htm).
- Thompson, G., Field, P.R., Rasmussen, R.M., Hall, W.D., 2008. Explicit forecasts of winter precipitation using an improved bulk microphysics scheme. Part II: implementation of a new snow parameterization. *Mon. Weather Rev.* 136, 5095–5115.
- Thurai, M., Gatlin, P.N., Bringi, V.N., 2016. Separating stratiform and convective rain types based on the drop size distribution characteristics using 2D video disdrometer data. *Atmos. Res.* 169, 416–423.
- Tong, M., Xue, M., 2005. Ensemble Kalman filter assimilation of Doppler radar data with a compressible nonhydrostatic model: OSS experiments. *Mon. Weather Rev.* 133, 1789–1807.
- Vendrasco, E.P., Sun, J., Herdies, D.L., De Angelis, C.F., 2016. Constraining a 3DVAR radar data assimilation system with large-scale analysis to improve short-range precipitation forecasts. *J. Appl. Meteorol. Climatol.* 55, 673–690.
- Wang, H., Sun, J., Fan, S., Huang, X.Y., 2013a. Indirect assimilation of radar reflectivity with WRF 3D-var and its impact on prediction of four summertime convective events. *J. Appl. Meteorol. Climatol.* 52, 889–902.
- Wang, H., Sun, J., Zhang, X., Huang, X.Y., Auligné, T., 2013b. Radar data assimilation with WRF 4D-Var. part I: system development and preliminary testing. *Mon. Weather Rev.* 141, 2224–2244.
- Wu, D., et al., 2013. Impacts of microphysical scheme on convective and stratiform characteristics in two high precipitation squall line events. *J. Geophys. Res. Atmos.* 118, 11119–1111358.
- Xiao, Q., Kuo, Y.-H., Sun, J., Lee, W.-C., Lim, E., Guo, Y.-R., Barker, D.M., 2005. Assimilation of Doppler radar observations with a regional 3DVAR system: impact of Doppler velocities on forecasts of a heavy rainfall case. *J. Appl. Meteorol.* 44, 768–788.
- Xu, K.M., 1995. Partitioning mass, heat, and moisture budgets of explicitly simulated cumulus ensembles into convective and stratiform components. *J. Atmos. Sci.* 52, 551–573.
- Xu, M., Sun, J., Liu, Y., Tessendorf, S., 2013. Radar data assimilation for the prediction of front range convection. In: 36th Conference on Radar Meteorology/Use of Radar Data for NWP Models: Radar Data Assimilation for NWP Model Initialization. American Meteorological Society, Breckenridge, CO, US.
- Yang, S., Smith, E.A., 2000. Vertical structure and transient behavior of convective-stratiform heating in TOGA COARE from combined satellite-sounding analysis. *J. Appl. Meteorol.* 39, 1491–1513.
- Yuter, S.E., Houze, R.A., 1995. Three-dimensional kinematic and microphysical evolution of Florida cumulonimbus. Part II: frequency distributions of vertical velocity, reflectivity, and differential reflectivity. *Mon. Weather Rev.* 123, 1941–1963.
- Zhang, J., Langston, C., Howard, K., 2008. Brightband identification based on vertical profiles of reflectivity from the WSR-88D. *J. Atmos. Ocean. Technol.* 25, 1859–1872.
- Zhang, F., Weng, Y., Sippel, J.A., Meng, Z., Bishop, C.H., 2009. Cloud-resolving hurricane initialization and prediction through assimilation of Doppler radar observations with an ensemble Kalman filter. *Mon. Weather Rev.* 137, 2105–2125.